VISIBLE AND INFRARED EMISSION FROM Er_2O_3 NANOPARTICLES, AND Ho^{+3}, Tm^{+3}, AND Sm^{+3} DOPED IN AlN FOR OPTICAL AND BIOMEDICAL APPLICATIONS

THESIS SUBMITTED FOR THE DEGREE

MASTER OF SCIENCE

BY

LYNDA L. WILKINSON

ADVISOR

DR. MUHAMMAD MAQBOOL

DEPARTMENT OF PHYSICS AND ASTRONOMY
BALL STATE UNIVERSITY
MUNCIE, INDIANA
JULY 2012

ABSTRACT

Light emission from optical materials play an important role in the optical devices fabrication, display technologies, laser and biomedical physics applications like laser surgeries, and cancer detection. These light emitting materials can be produced in the form of thin films, nanoparticles, and quantum wells. Rare-earth elements and transition metals are famous for their light emission in ultraviolet, infrared, and visible range. These materials have been used by many investigators, and a number of useful devices are invented based on the emission of light from these rare-earth elements and transition metals.

Moreover, infrared light have been in use in laser surgeries and cancer detection due to its high penetration ability inside the human body. We have investigated some rare-earth ions holmium (Ho^{+3}), Thulium (Tm^{+3}), and Samarium (Sm^{+3}) for infrared emission and their possible biomedical applications. Ho^{+3} and Tm^{+3} are already in use for biomedical applications due to their infrared emission. However, the host materials where these ions are doped in are expensive with little stability. We are using amorphous aluminum nitride (AlN) as host material. Due to its high stability, less expensive, and easily producible nature, AlN will serve one of the best hosts for such rare-earth ions and will improve the use of the mentioned rare-earth ions in laser surgeries and cancer detection. The rare-earth ion holmium (Ho^{+3}) had two emission peaks that were observed around 825 nm and 1537 nm. The infrared emission at 825 nm was obtained as a result of $^5S_2 \rightarrow {}^5I_7$ transition,

and the infrared emission at 1537 nm was obtained as a result of $^{5}S_2 \rightarrow {}^{5}I_5$ transition. The rare-earth ion samarium (Sm^{+3}) had two emission peaks that were observed around 936 nm and 1863 nm. The rare-earth ion thulium (Tm^{+3}) had three emission peaks that were observed around 824 nm, 1293 nm, and 1891 nm. The infrared emission at 824 nm was obtained as a result of $^{3}H_4 \rightarrow {}^{3}H_6$ transition, the infrared emission at 1293 nm was obtained as a result of $^{3}H_5 \rightarrow {}^{3}H_6$ transition and the infrared emission at 1891 nm was obtained as a result of $^{3}F_4 \rightarrow {}^{3}H_6$ transition.

Light emitting nanoparticles are getting special attention due to their use in optical technology and biomedical applications. The present work reports light emission from Erbium Oxide nanoparticles. The nanoparticles, with 43 nm diameter, were obtained in the form of nanopowder with 99.9% purity. These nanoparticles were characterized for their light emission under a 532 nm Nd:YAG laser excitation. A Photoluminescence (PL) system, made by Princeton Instrumentation, was used to detect fluorescence emission from the nanoparticles. The PL system consisted of Pixis brand CCD camera with a range of 300 to 2000 nm. The Erbium Oxide nanoparticles were also mixed in distilled water to obtain spectrum. Two emission peaks were observed around 554 nm and 813 nm from the Erbium Oxide nanoparticles. The green emission at 554nm was obtained as a result of $^{4}I_{15/2} \rightarrow {}^{4}S_{3/2}$ transition, and the near infrared emission from $^{4}I_{15/2} \rightarrow {}^{4}I_{13/2}$ transition. The process was also repeated in vacuum and it was found that the green emission enhances tremendously when the nanoparticles are excited in vacuum. This enhanced luminescence

from the Erbium Oxide nanoparticles shows their potential importance in the optical devices and Biomedical applications.

Dedication

This work is dedicated to my husband Jerold Wilkinson who has supported me throughout my endeavor to earn a Bachelor's Degree and a Master's Degree in Physics. The entire process would not have been possible without your loving support. You applauded me when I succeeded and urged me to work harder when I failed. Thank you for the years of hard work, love, and support that you have given to me. All my thanks are not enough to repay my debt to you. I love you.

ACKNOWLEDGEMENTS

I would like to thank my husband Jerold Wilkinson for his support throughout my education. He made my educational journey possible through emotionally and financially supporting me. I cannot begin to thank him enough for all that he has done for our family. This master's degree is for him as much as it is for me.

In addition to my husband, many other family members need to be mentioned as they have given me countless hours of support. My mother-in-law and father-in law, Wade Wilkinson and Margaret "Peggy" Wilkinson made sure my daughters came home from school safely each day. I would like to thank my two daughters Ginger and Ruthie for putting up with their Mommy being absent many evenings, and being very busy other evenings when she was home. I love you all very much.

I would also like to thank Chris E. Wagner who helped me understand many difficult concepts and homework problems in my master's classes. Chris is a great teacher. I have been blessed by knowing him. I am truly grateful for having him as a friend.

I am especially in debt to The Indiana Academy for Science, Mathematics, and Humanities for the opportunity to teaching Precalculus while finishing my thesis. Also, The Indiana Academy faculty members Dr. Franklin Shobe and Dr. George Devendorf for their assistance and instruction in statistical error analysis and its use on my data. Also, Dr. Margaret Smith of the Indiana Academy for proofreading my thesis and suggestion grammatical corrections.

I would like to thank Anderson University's Department of Chemistry and Physics for the use of their X-Ray Fluorescence instrument, especially Dr. Chad Wallace, Dr. Scott Carr and Dr. Dale Bales for their guidance in the use of the instrument.

I would like to thank group collaborators, Dr. Martin Kordesch at Ohio University for doing the photoluminescence spectrometry under a vacuum on the Erbium Oxide nanoparticles, and Iftikhar Ahmad at Markland University, Pakistan. Lastly, I would like to thank my advisor and all the professors I've had during my time here at Ball State University. Without you, this wouldn't have been possible! I would like to thank all the professors who taught me at Ball State University. I would like to thank you for understanding my unusual circumstances and working with me to overcome them. I would like to thank my advisor Dr. Muhammad Maqbool for all the help he has given me on this thesis.

Table of Contents

List of Figures

Figure **Page**

List of Tables

Table **Page**

Chapter 1

1.1 Introduction

Nitride semiconductors doped with rare-earth elements have been investigated for potential utilization in several areas. These areas of utilization are display technologies, biomedical field, device fabrication, and for their lasing properties [1-4]. Nitride semiconductors have several characteristic qualities. The characteristic qualities, which have been found AlN are high thermal conductivity, chemical inertness, and stability. Research into rare-earth elements has found utilizable qualities such as: thermal, electrical, optical, and photonics uses. When AlN is utilized as host lattice in the semiconductor, it becomes transparent in visible, UV, and IR wavelength emissions, due to wide bandgap of 210 nm. Therefore AlN was selected as a host lattice for the rare-earth elements in this study [5-10].

When a semiconductor is doped with a rare-earth element, it is possible to detect sharp emission lines when using a spectrometer. The rare-earth elements chosen for this

study were holmium, thulium, samarium, and erbium oxide (Er_2O_3) nanoparticles. These rare-earth elements were chosen because they produce sharp-line emissions when excited by a laser during photoluminescence spectroscopy. Photoluminescence is the type of spectroscopy utilized in this study, on the samples of holmium, thulium; samarium doped into an Aluminum Nitride (AlN) thin film and erbium oxide (Er_2O_3) nanoparticles. According to Wikipedia:

> "Photoluminescence (PL) is a process in which a substance absorbs photons (electromagnetic radiation) and then re-radiates photons. Quantum mechanically, this can be described as an excitation to a higher energy state and then a return to a lower energy state accompanied by the emission of a photon. This is one of many forms of luminescence (light emission) and is distinguished by photoexcitation (excitation by photons), The period between absorption and emission is typically extremely short, in the order of 10 nanoseconds. Under special circumstances, however, this period can be extended into minutes or hours" [11].

A CCD camera inside the spectrometer then detects the emissions and depicts them in a graphical format of wavelength verses arbitrary intensity.

There are four common types of nitride semiconductors. These four types of semiconductors are indium nitride, boron nitride, gallium nitride and aluminum nitride. The Aluminum Nitride (AlN) host was chosen due to its wide band-gap of 210 nm [5-10]. The lasers used in this study were a 532 nm Nd:YAG laser and a 783 nm crystal laser. The energy levels of rare-earth elements have been known for many years and

were used for comparison and identification of the sharp-line emission peaks of our samples [14]. In this study we explored the energy level transitions of the rare-earth elements holmium, thulium, and samarium doped into an AlN thin film, as well as the energy level transitions of erbium oxide (Er_2O_3) nanoparticles by photoluminescence spectroscopy.

Chapter 2

2.1 Semiconductors

A semiconductor is a material that exhibits an electrical conductivity that is an intermediate between the electrical conductivity of a conductor and of an insulator (a non-conductor). In order for any material to conduct an electrical current, a mobile charge carrier (MCC) must be present within that material. A mobile charge carrier (MCC) can be an ion, an electron, or both, and is free to move within the material [37]. However, ionic conduction can make changes in the composition of the material and will not be considered in this study.

Most metals are good conductors and their resistance to the current increases as the temperature increases. The resistance in an insulator (non-conductor) is many times greater than in a conductor. In a semiconductor, as the temperature increases, the resistivity decreases rapidly (thermal conductivity) and at low temperatures the semiconductor as like an insulator. Also, the conductivity of a semiconductor is typically

sensitive to light, with a lower conductivity in the dark as compared to when it is illuminated [15].

Historically, semiconductors have been used in electronics, and are best known in that capacity. The two semiconductors most often utilized in electronics are Germanium (Ge) and Silicon (Si). There is another classification of semiconductors that have been utilized in the field of optics. These semiconductors are the III-Nitride semiconductors and have been investigated not only for their electrical conductivity, but for their optical properties as well.

2.2 III-Nitride Semiconductors

The III-Nitride semiconductor materials are Gallium Nitride (GaN), Aluminum Nitride (AlN), Indium Nitride (InN), and Boron Nitride (BN). The III-Nitride semiconductors have several traits that make them attractive as thin film host for luminescent materials. These traits include their energy band-gap, a high thermal conductivity, and a high melting point. Each of these of the III-Nitride semiconductors exhibits unique values for each of these traits.

Typically, III-Nitride semiconductors are grown in a process called magnetron sputtering. This process can result in several types of crystalline lattices. The different crystalline lattices are a result of the temperature maintained during the growth process. The types of crystalline lattices observed in III-Nitride semiconductors are wurtzite, hexagonal, rhombohedral, rock-salt, and zinc blende [16].

2.3 Gallium Nitride

Since the 1990's, Gallium nitride (GaN) has been used in bright-light emitting diodes. In the subsequent years following the 1990's, GaN has been used to make violet (405 nm) laser diodes, due to its large energy band-gap of 3.39 eV (366 nm) [17]. The physical properties of GaN can be found in the Table 2.1 below.

Table 2.1 *Gallium Nitride Physical Properties [17].*

Gallium Nitride		
Crystal Structure	Wurtzite	Zinc Blend
Energy Band-Gap (eV)	3.39	3.2
Energy Band-Gap (nm)	366	388
Melting Point (°C)	>2500	>2500
Thermal Conductivity (W cm^{-1} $°C^{-1}$)	1.3	1.3

2.4 Aluminum Nitride

In 1877 AlN was first synthesized. It wasn't until the mid 1980's that it was investigated for utilization in microelectronics because of its high thermal conductivity [18]. At high temperatures, AlN is stable in inert atmospheres. Uses for AlN include optio-electronics, dielectrics, substrates where a high thermal conductivity is required, and in steel and semiconductor manufacturing [18]. The physical properties of AlN can be found in the Table 2.2 below.

Table 2.2 *Aluminum Nitride Physical Properties [17].*

Aluminum Nitride	
Crystal Structure	Wurtzite
Energy Band-Gap (eV)	6.2
Energy Band-Gap (nm)	200
Melting Point (°C)	2750 (between 100 – 500 atm Nitrogen)
Thermal Conductivity (W cm^{-1} $°C^{-1}$)	2.85

2.5 Indium Nitride

Indium Nitride (InN) is a semiconductor material with possible applications in high-speed electronics and solar cells. It has a small band-gap with the absolute band gap being 1.9eV depending on temperature [19]. The physical properties of InN can be found in the Table 2.3 below.

Table 2.3 *Indium Nitride Physical Properties [17].*

Indium Nitride	
Crystal Structure	Wurtzite
Energy Band-Gap (eV)	1.9 – 2.05
Energy Band-Gap (nm)	605 - 653
Melting Point (°C)	Exponential range depending on pressure
Thermal Conductivity (W cm^{-1} $°C^{-1}$)	0.45

2.6 Boron Nitride

Boron nitride is not a naturally occurring substance and has to be made from boric acid or boron trioxide. It has excellent thermal and chemical stability and has been used in ceramics and in high temperature equipment [20]. The physical properties of BN can be found in the Table 2.4 below.

Table 2.4 *Boron Nitride Physical Properties [17].*

Boron Nitride			
Crystal Structure	Wurtzite	Zinc Blend	Hexagonal

Energy Band-Gap (eV)	4.5 - 5.5	6.1 - 6.4	4.0 - 5.8
Energy Band-Gap (nm)	225.5 - 275.5	193.8 - 2.3.3	213.8 - 310
Melting Point (°C)			
Thermal Conductivity (W cm^{-1} $°C^{-1}$)		7.4	

Chapter 3

3.1 Rare-Earth Elements

Rare earth elements are a group of elements on the periodic table of elements. The “rare earths” consist of yttrium and the 15-lanthanide elements, excluding scandium [21]. The energy levels associated with the 4f electrons and transitions are of particular interest because they are responsible for the emissions examined in this study. The electron configuration associated with each of the rare earth elements can be seen in Table 3.1.

Table 3.1 *Electronic Configuration of the Rare Earths [21].*

Solid or Liquid State (Real life) Configuration				
Normal			Unusual	
Element	**No. 4f Electrons**	**No. Valence Electrons**	**No. 4f Electrons**	**No. Valence Electrons**
Er	**11**	**3**	**- -**	**- -**
Ho	**10**	**3**	**- -**	**- -**
Sm	**5**	**3**	**6**	**2**
Tm	**12**	**3**	**- -**	**- -**

(*The term "unusual" is used in the sense that it is unusual from the point of view of the rare earths as a whole, rather than from a particular element's point of view.)

3.2 Erbium, Holmium, Thulium, and Samarium

The four rare-earth elements studied include Holmium (Hm), Thulium (Tm), and Samarium (Sm). To date, little analysis on these rare-earth elements with a AlN semiconductor has been completed. The electron orbital properties were found in table 3.1. The basic properties of these three rare-earth elements are shown below in Table 3.2, followed by figure 3.1, which shows the lowest energy levels of the three-valence ions as determined from the crystal absorption and fluorescence spectra [22, 23].

Table 3.2 *Some Atomic Constants, and Properties, of Rare Earth Elements* [23].*

Property	Rare Earth Element			
	Erbium (Er)	Holmium (Hm)	Thulium (Tm)	Samarium (Sm)
Melting Point (°C)	1529	1474	1545	1077
Boiling Point (°C)	2863	2695	1947	1792
S	1.5	2	1	2.5
L	6	6	5	5
J	7.5	8	6	2.5

The 4f shell of each rare-earth element has the capability of different transitions. These transitions are responsible for the emissions in which this research was most interested.

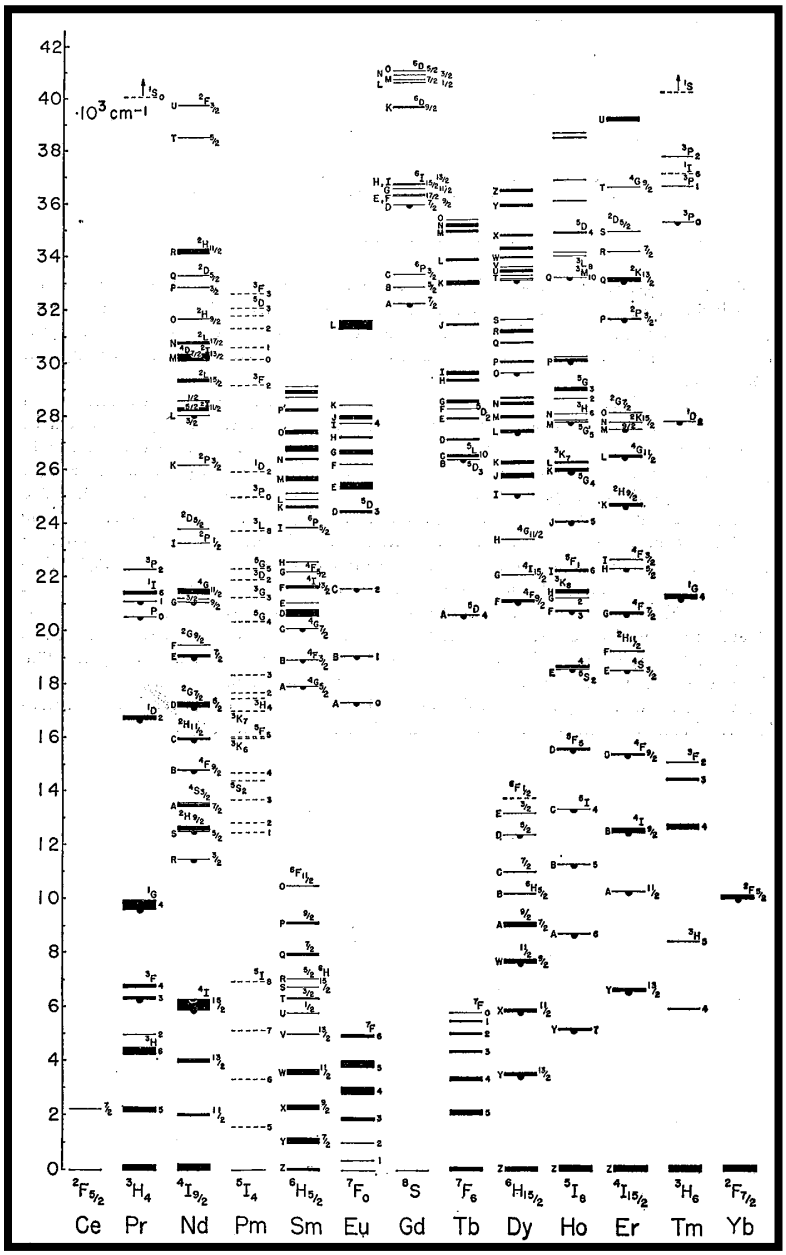

Figure 3.1 Lowest Energy Levels of the three-valence ions as determined by the crystal absorption and fluorescence spectra [23].

3.3 Nanoparticles in Cancer Detection

It is common knowledge that the detection and treatment of cancer is difficult. Sometimes the treatment can be almost as bad as the cancer itself. The commonly used methods of detection of cancer cells can affect healthy cells around the cancerous ones. A subgroup of nanotechnology is now being utilized in the study of cancer detection in mice [24]. These nanoparticles have presented a new problem for the researchers: the nanoparticles' size are causing a problem. The particles are so small that they are passing through the healthy cells around the cancerous cells, and causing the healthy cells to mutate into cancerous cells. This issue has to be solved before the nanoparticles could be used in human studies.

There are two main types of nanoparticles being studied in the detection of cancer cells. The first type of nanoparticles are gold nanoparticles. The gold nanoparticles attach themselves to a protein found in cancer cells called Epidermal Growth Factor Receptor (EGFR). The gold nanoparticles are put into a conjugated nanoparticle solution. The solution is then put onto the healthy cells as well as the cancerous cells. The area is then examined with a normal microscope. The gold nanoparticles bond with the cancerous cells and can be viewed with a microscope. The cancerous cells look shiny due to the bonding with the gold nanoparticles, as opposed to the healthy cells, which do not look shiny. This method makes the detection of cancer very easy, as the cancerous cells visually stand out from the healthy cells [24, 25].

The second type of nanoparticles being studied for cancer detection are magnetic iron oxide nanoparticles. These particles are encased in a "biocompatible material"

which sticks to the tumor. The tumor cells then act as magnets and can be attracted to a biopsy needle, making their removal simpler [24, 25].

Chapter 4

4.1 Methodology and Experimental Setup

Thin Films

The thin films used in this study were grown in an RF magnetron-sputtering chamber at Ohio University's Surface Science Laboratory, in Athens Ohio. The thin films used in this study were AlN:Ho, AlN:Sm, and AlN:Tm. These thin films were grown on a thin silicon wafer in a RF magnetron-sputter chamber at 77K. The doping of the rare-earth elements was achieved by drilling a hole into the 99.99% pure aluminum target. The aluminum target was 5.1 cm in diameter and the hole that was drilled was 0.5 cm in diameter. After the hole was drilled into the target, the hole was then filled with the particular rare-earth element in which the film was to be doped.

The power of the sputter chamber was between 100 and 200 watts. The pressure inside the sputter chamber was kept below 0.00003 Torr, at a constant temperature of

77K, in a nitrogen atmosphere. The films were grown until they reached a thickness between 100 nm and 500 nm, as measured with a quartz crystal thickness monitor in the growth chamber. X-ray diffraction (XRD) was used to determine the structure of the films, with all films being amorphous.

Princeton Instruments manufactured the spectrometer used for photoluminescence in this research. The model number of the spectrometer was SP2300i and the spectrometer was used in union with software called Winspec.

Each sample was mounted onto an apparatus that allowed rotation upon an axis, but at a fixed height. The mounted sample was kept at the same height as the opening of the slit of the spectrometer. The two lasers used for excitation were a 532nm Nd:YAG green solid state laser and 783nm infrared solid state crystal laser.

All thin film experiments used an identical setup: the laser, film, and slit opening to the spectrometer were set at identical angles. An approximate angle of 40° was used relative to the laser with respect to the film. This subsequently produced an angle of 10° with respect to the detector relative to the normal. An overview of this setup is shown in Figure 4.1 and a photograph of the setup in Figure 4.2. All data which was taken was recorded into a Microsoft Excel spread sheet for analysis.

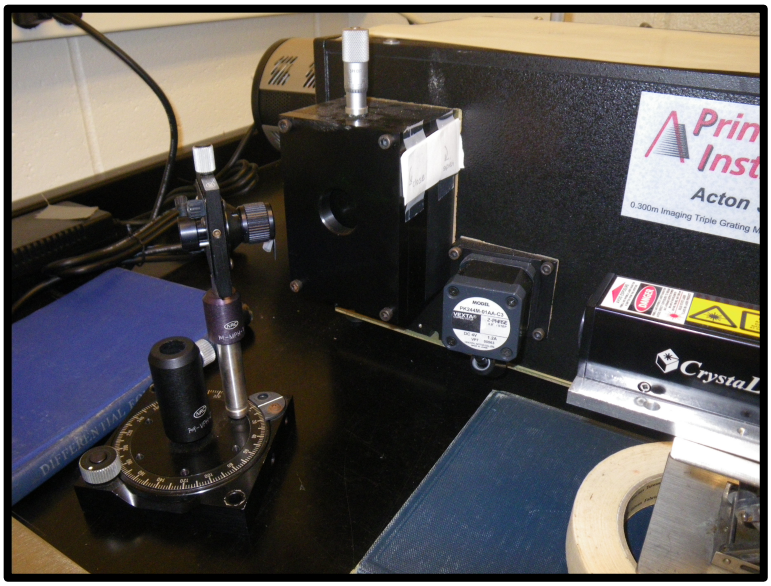

Figure 4.1 Photograph of experimental setup for thin film analysis.

X-ray Fluorescence Spectroscopy (XRF) at Anderson University was also utilized to analyze the thin films. The instruments utilized for this analysis were manufactured by the Amptek Corporation and assembled by Dr. Dale Bales.

Nanoparticles

The Erbium Oxide Nanoparticles (Er_2O_3) utilized in this study were prepared by and obtained from Nanostructured and Amorphous Materials, Inc. based in Los Alamos, New Mexico, USA. The size of each nanoparticle is 43 nm and they are nearly spherical. The nanoparticles/nanopowder are 99.9% pure and are pink in color.

Three experimental setups were utilized in this study:

1. The nanoparticles were suspended in a small glass vial of water. The laser was then shined straight through the solution to the spectrometer as shown in Figure 4.3.

2. The nanoparticles were adhered to Scotch brand tape, with the tape ends fixed to a large diameter circular frame. The same setup was used as in the thin films study, which was described above in section 4.1.
3. The nanoparticles were examined by photoluminescence (PL) spectrometry under a vacuum at Ohio University, in Athens Ohio. A 488 nm Argon laser was used to obtain the photoluminescence spectra at a low pressure of 10^{-6} torr (vacuum), analyzed by a spectrometer equipped with a cooled photomultiplier tube. The power of the laser was 9.3 mW.

Figure 4.2 Experimental setup for nanoparticles suspended in water in a small glass vial.

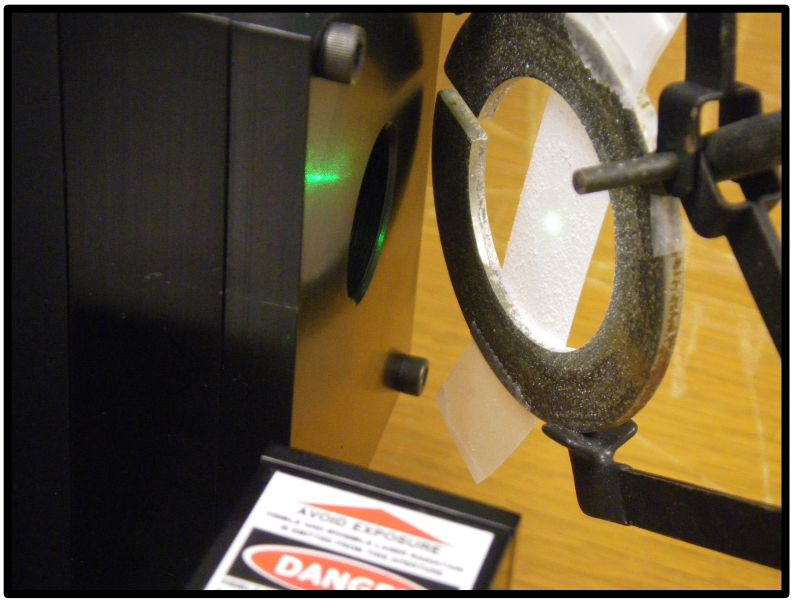

Figure 4.3 Experimental setup for nanoparticles adhered to Scotch tape held by a circular frame.

4.2 Resolution and Error Analysis

Statistical error analysis was completed using the T-test as outlined by Allan G. Bluman in *Elementary Statistics: A Step by Step Approach* [26, 27]. The standard error and P-Value for each spectrum was found. The equations used are shown below (equations 4.1-4.8).

Population Mean: $$\mu = \frac{\Sigma X}{N} \tag{4.1}$$

Sample Mean: $$\overline{X} = \frac{\Sigma X}{n} \tag{4.2}$$

Variance: $$\sigma^2 \equiv \overline{X} - \mu^2 \tag{4.3}$$

Sample Variance $$s^2 = \frac{\Sigma\left(X - \overline{X}\right)}{n-1} \tag{4.5}$$

Population Standard Deviation: $$\sigma = \sqrt{\sigma^2} \quad (4.6)$$

Sample Standard Deviation: $$s = \sqrt{\frac{\Sigma(X - \overline{X})}{n-1}} \quad (4.7)$$

T-test $$t = \frac{\overline{X} - \mu}{s/\sqrt{n}} \quad (4.8)$$

Where μ is the population mean, $\overline{X}$ is the sample mean, σ is the population standard deviation, σ^2 is the population variance, t is the standard error, s is the sample standard deviation, n represents the total number of values in the sample, and N represents the total number in the population. The t-test was utilized to find the standard error on each emission line of each spectrum. The P-Value was found from a table in Bluman [26, 27].

The p-value is the probability of obtaining a test statistic as least as extreme as the one that was actually observed, assuming that the null hypothesis is true [26, page 383]. The null hypothesis (symbolized by H_0) is a statistical hypothesis that states that there is no difference between a parameter and a specific value or that there is no difference between two parameters [26, page 367]. The null hypothesis is rejected when the p-value is less than the significance level of 0.05. When the null hypothesis is rejected, the result is said to be statistically significant. In this study the null hypothesis is that there is no difference between our data and data arrived at by chance.

Chapter 5

5.1 Results and Analyses

Silicon Wafer

Analysis of a silicon (Si) was preformed in order to subtract the silicon peaks from the spectrum of the samples used in this study. The photoluminescence analysis of a plain silicon wafer shows emission peaks at 805 nm, 1059 nm, 1620 nm, 2124 nm and 2431 nm. These peaks were found in all of the samples in this study, and they were considered as peaks due to the silicon and were dismissed. Figure 5.1 show the 805 nm, 1059 nm, 1620 nm, 2124 nm and 2431 nm peaks for the silicon wafer respectively.

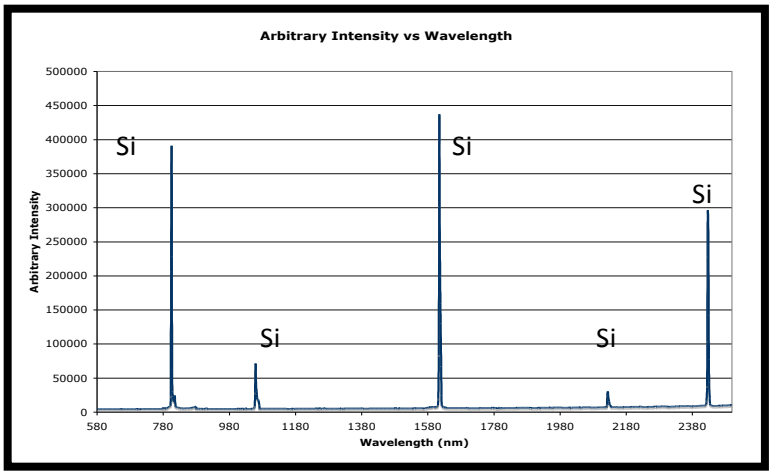

Figure 5.1 The peaks for Silicon (Si). The y-axis is in units of arbitrary intensity units (A.I.U.).

5.2 Holmium

The photoluminescence analysis shows that AlN:Ho^{+3} emits at 825 nm, and 1537 nm, when excited by a 532 nm Nd:YAG laser and 783 nm crystal laser. Figure 5.2 and Figure 5.3 show the 825 nm and the 1537 nm peaks for Ho^{+3}. These peaks correspond to $^5S_2 \rightarrow {}^5I_7$ and $^5S_2 \rightarrow {}^5I_5$ respectively [30].

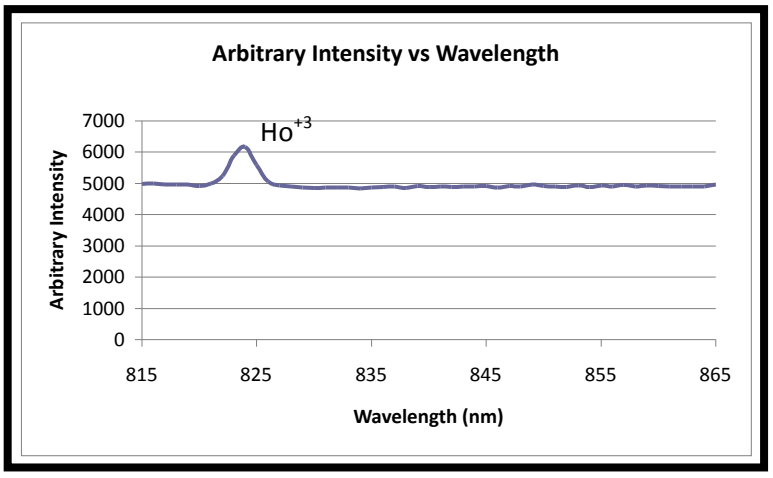

Figure 5.2 The 825 nm peak for Ho^{+3}. The y-axis is in units of arbitrary intensity units (A.I.U.).

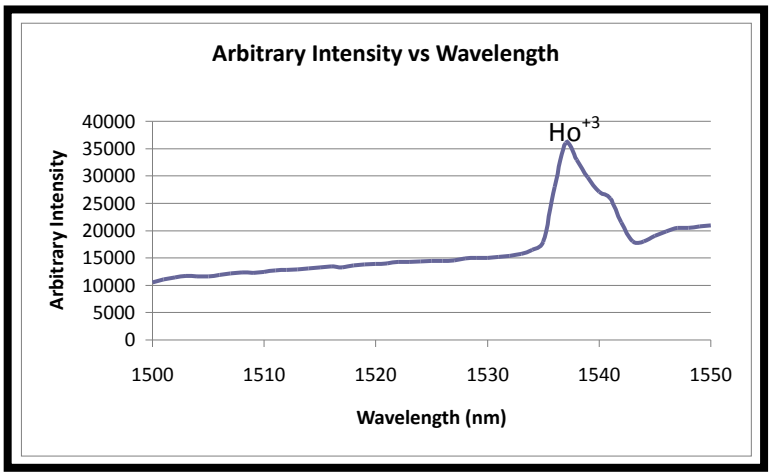

Figure 5.3 The 1537 nm peak for Ho^{+3}. The y-axis is in units of arbitrary intensity units (A.I.U.).

Table 5.1 Statistical Analyses Data for AlN:Ho^{+3}.

Emission Wavelength λ (nm)	**825 nm**	**1537 nm**
Sample Size (n) [runs]	19	9
Standard Error (t)	8.64	5.82
P-Value (p)	8.01×10^{-8}	3.97×10^{-4}
Mean (A.I.U.)	8226	27886
Standard Deviation (s) (A.I.U.)	4148	14378
Interval (95%) (A.I.U.)	(6227, 10226)	(16834, 38938)
Null Hypothesis (H_0)	REJECT	REJECT

The statistical error analysis of the AlN:Ho^{+3} sample showed the peaks at 825 nm and 1537 nm were all statistically significant.

Analyses of the AlN:Ho by X-Ray Fluorescence Spectroscopy (XRF) was done in order to show the presence of Ho^{+3} in the sample. The analyses of the AlN:Ho^{+3} thin film by X-Ray Fluorescence Spectroscopy (XRF) showed a peak at 6.72 keV, which verifies the presence of Holmium (Ho) in the AlN:Ho^{+3} sample. See Figure 5.4.

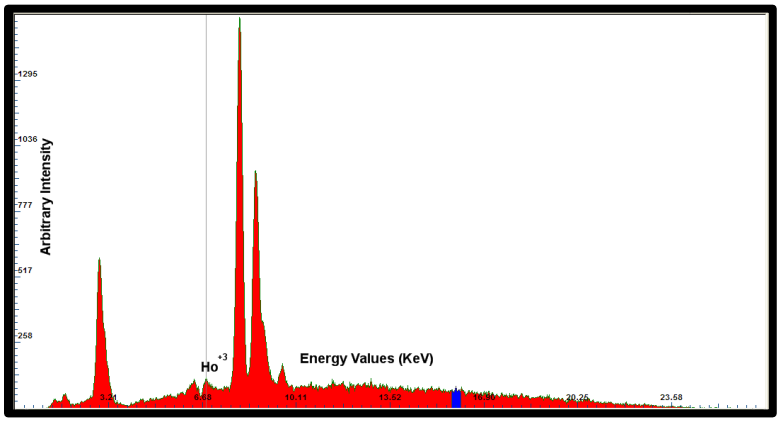

Figure 5.4 X-Ray Fluorescence (XRF) spectrum showing the presence of Holmium (Ho) in the AlN:Ho^{+3} sample. The vertical line is to help identify the peak for Ho at 6.72 KeV. The y-axis is in units of arbitrary intensity units (A.I.U.). The x-axis is in units of energy values (KeV).

5.3 Samarium

The photoluminescence analysis shows that AlN:Sm^{+3} emits at 936 nm, and 1863nm, when excited by a 532 nm Nd:YAG laser and 783 nm crystal laser. Figure 5.5 and Figure 5.6 show the 936 nm and the 1863 nm peaks for Sm^{+3}.

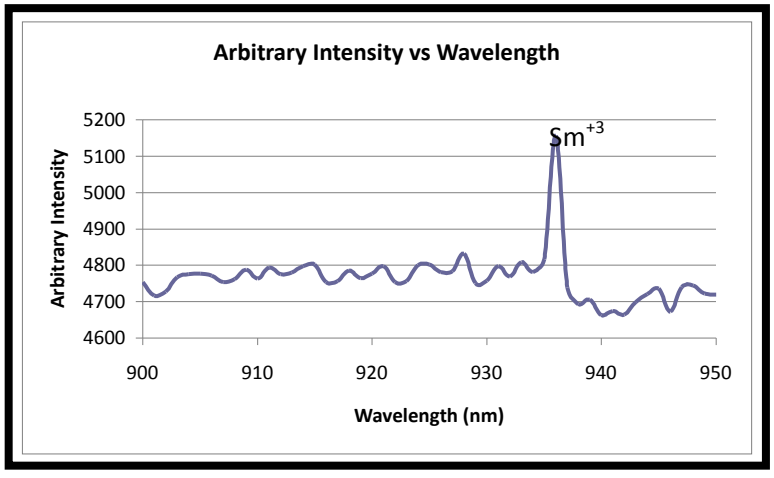

Figure 5.5 The 936 nm peak for Sm^{+3}. The y-axis is in units of arbitrary intensity units (A.I.U.).

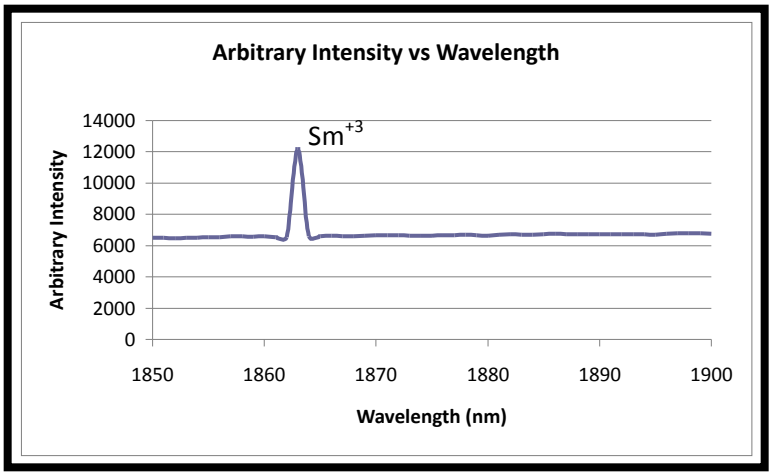

Figure 5.6 The 1863 nm peak for Sm^{+3}. The y-axis is in units of arbitrary intensity units (A.I.U.).

Table 5.2 Statistical Analyses Data for AlN:Sm^{+3}.

Emission Wavelength λ (nm)	936 nm	1863 nm
Sample Size (n) [runs]	5	5
Standard Error (t)	39.68	78.81
P-Value (p)	0.000002	0.0000002
Mean (A.I.U.)	5248	6328
Standard Deviation (s) (A.I.U.)	296	180
Interval (95%) (A.I.U.)	(4881,5616)	(6105,6551)
Null Hypothesis (H_0)	REJECT	REJECT

The statistical error analysis of the AlN:Sm sample showed the peaks at 936 nm, and 1863 nm was statistically significant.

Analyses of the AlN:Sm^{+3} sample by X-Ray Fluorescence Spectroscopy (XRF) was done in order to show the presence of Samarium (Sm) in the AlN:Sm^{+3} sample. The analyses of the AlN:Sm^{+3} thin film by X-Ray Fluorescence Spectroscopy (XRF) showed a peak at 5.64keV, which verifies the presence of Samarium (Sm) in the AlN:Sm^{+3} sample. See Figure 5.7.

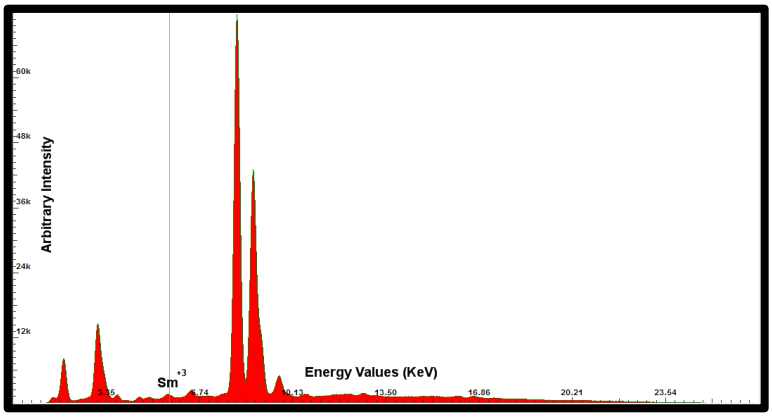

Figure 5.7 X-Ray Fluorescence (XRF) spectrum showing the presence of Samarium (Sm) in the AlN:Sm^{+3} sample. The vertical line is to help identify the peak for Sm at 5.64 KeV. The y-axis is in units of arbitrary intensity units (A.I.U.). The x-axis is in units of energy values (KeV).

5.4 Thulium

The photoluminescence analysis shows that AlN:Tm^{+3} emits at 824 nm, 1293 nm, and 1891 nm, when excited by a 532 nm Nd:YAG laser and 783 nm crystal laser. Figure 5.8, Figure 5.9, and Figure 5.10 show the 824,nm, 1293 nm and the 1891 nm peaks for Tm^{+3}. These peaks correspond to $^3H_4 \rightarrow {}^3H_6$, $^3H_5 \rightarrow {}^3H_6$, and $^3F_4 \rightarrow {}^3H_6$ respectively [30].

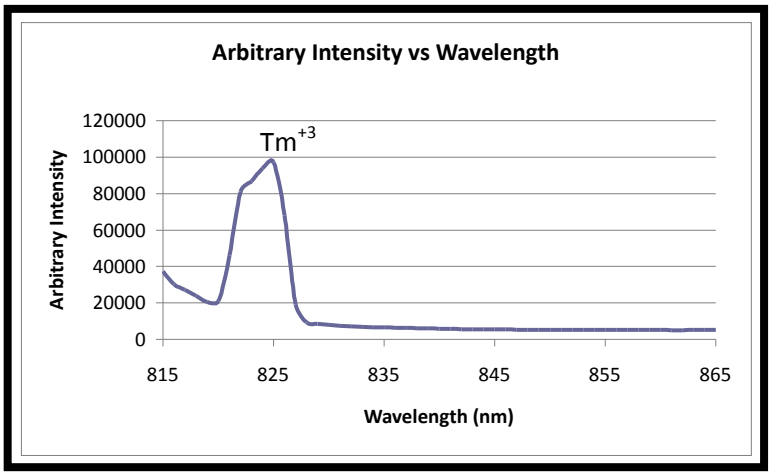

Figure 5.8 The 824 nm peak for Tm^{+3}. The y-axis is in units of arbitrary intensity units (A.I.U.).

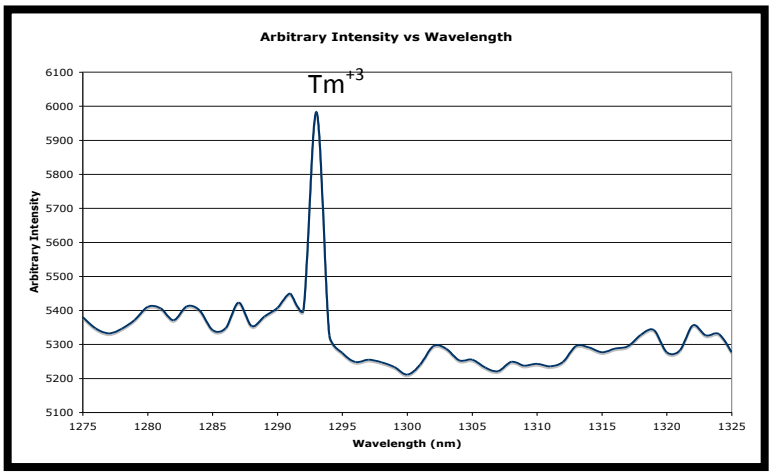

Figure 5.9 The 1293 nm peak for Tm^{+3}. The y-axis is in units of arbitrary intensity units (A.I.U.).

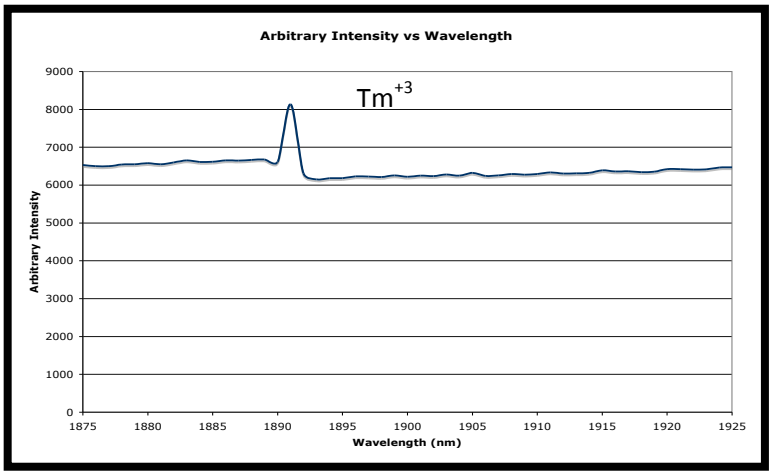

Figure 5.10 The 1891 nm peak for Tm^{+3}. The y-axis is in units of arbitrary intensity units (A.I.U.).

Table 5.3 Statistical Analyses Data for AlN:Tm^{+3}.

Emission Wavelength λ (nm)	**824 nm**	**1293 nm**	**1891 nm**
Sample Size (n) [runs]	5	5	5
Standard Error (t)	2.997	5.95	40.84
P-Value (p)	0.04	0.004	2.12×10^{-6}
Mean (A.I.U.)	259193	6236	7668
Standard Deviation (s) (A.I.U.)	193338	2342	420
Interval (95%) (A.I.U.)	(19132, 499254)	(3328, 9144)	(7147, 8188)
Null Hypothesis (H_0)	**REJECT**	**REJECT**	**REJECT**

The statistical error analysis of the sample showed the peaks at 824 nm, 1293 nm, and 1891 nm were statistically significant.

Analyses of the AlN:Tm^{+3} by X-Ray Fluorescence Spectroscopy (XRF) was done in order to show the presence of Thulium (Tm) in the AlN:Tm^{+3} sample. The analyses of the AlN:Tm^{+3} thin film by X-Ray Fluorescence Spectroscopy (XRF) showed a peak at 7.18keV, which verifies the presence of Thulium (Tm) in the AlN:Tm^{+3} sample. See Figure 5.11.

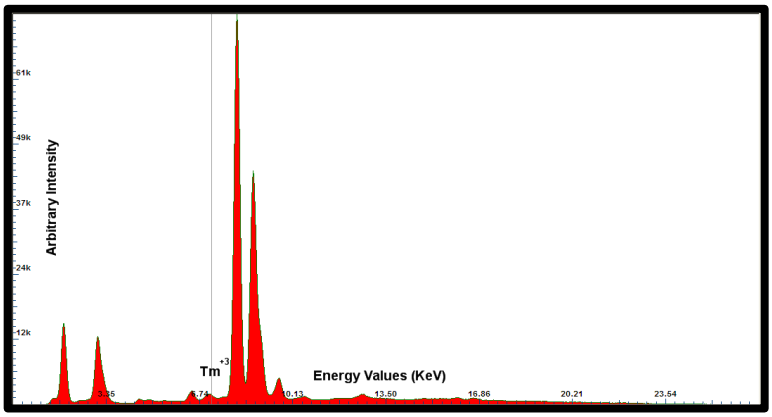

Figure 5.11 X-Ray Fluorescence (XRF) spectrum showing the presence of Thulium (Tm) in the AlN:Tm^{+3} sample. The vertical line is to help identify the peak for Tm at 7.18 KeV. The y-axis is in units of arbitrary intensity units (A.I.U.). The x-axis is in units of energy values (KeV).

5.5 Erbium Oxide Nanoparticles

Er_2O_3 Nanoparticles Suspended in Water

The photoluminescence analysis shows that Er_2O_3 Nanoparticles emit at 564 nm, 603 nm, and 814 nm when excited by a 532 nm Nd:YAG laser and 783 nm crystal laser.

Figure 5.11, Figure 5.12, and Figure 5.13 show the 564 nm, 603 nm, and 814 nm peaks for Er_2O_3 Nanoparticles . These peaks correspond to $^4I_{15/2} \rightarrow {}^4S_{3/2}$, $^4I_{15/2} \rightarrow {}^4F_{9/2}$ and $^4I_{15/2} \rightarrow {}^4I_{13/2}$ respectively [31, 32].

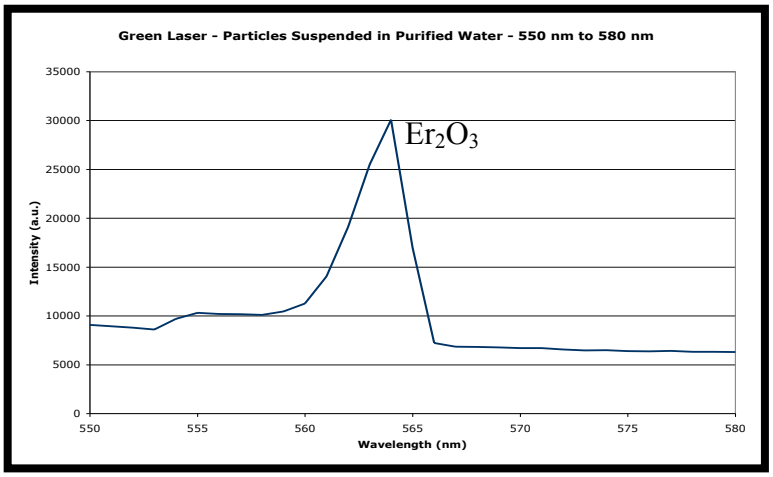

Figure 5.12 The 564 nm peak for Erbium Oxide (Er_2O_3) suspended in water. The y-axis is in units of arbitrary intensity units (A.I.U.).

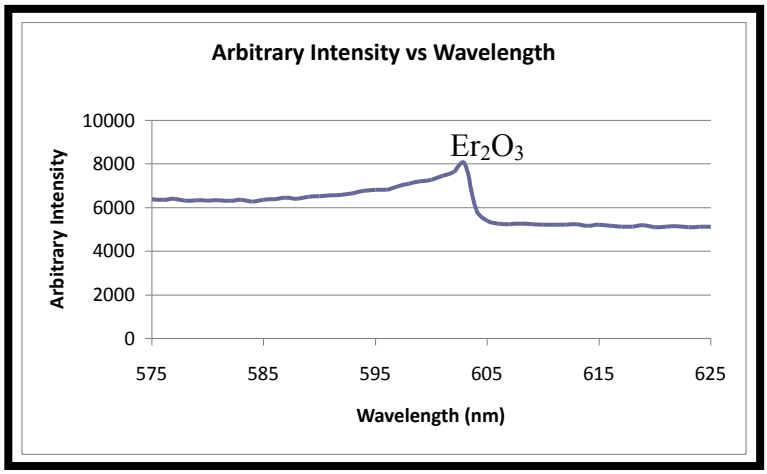

Figure 5.13 The 603 nm peak for Erbium Oxide (Er_2O_3) suspended in water using the 532 nm excitation laser. The y-axis is in units of arbitrary intensity units (A.I.U.).

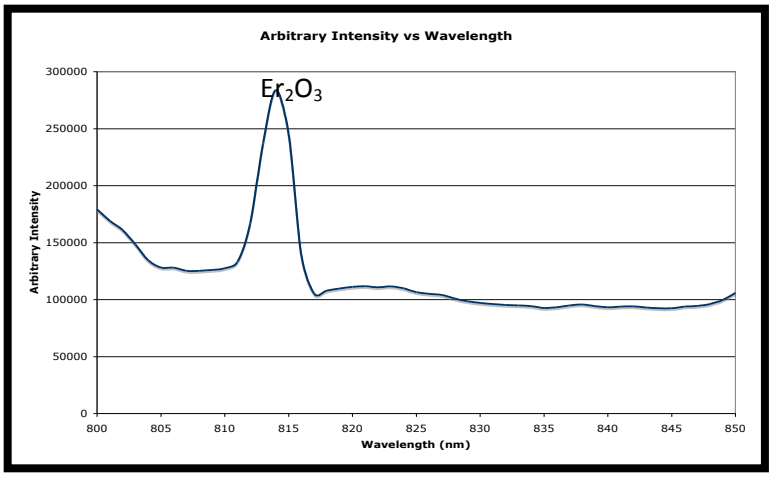

Figure 5.14 The 814 nm peak for Erbium Oxide (Er_2O_3) suspended in water using the 783 nm excitation laser. The y-axis is in units of arbitrary intensity units (A.I.U.).

Table 5.4 Statistical analyses data for nanoparticles suspended in water.

Emission Wavelength λ (nm)	**564 nm**	**603 nm**	**814 nm**
Sample Size (n) [runs]	2	6	5
Standard Error (t)	1.09	4.159	1101.72
P-Value (p)	0.308	0.0088	4.07×10^{-12}
Mean (A.I.U.)	63387	21346	144348
Standard Deviation (s) (A.I.U.)	47107	12571	320457
Interval (95%) (A.I.U.)	$(-3.6 \times 10^5, 4.9 \times 10^5)$	(8153, 34539)	$(-1.99 \times 10^5, 480647)$
Null Hypothesis (H_0)	ACCEPT	REJECT	REJECT

The statistical error analysis of the sample showed the peaks at 603 nm and 814 nm were statistically significant. However, the peak at 564 nm was not statistically significant and was most likely due to chance. It may however become significant with a larger sample size; therefore it was included in the data.

Scotch Brand Tape

Analysis of Scotch Brand Tape utilized as a host was performed in order to subtract the Scotch Brand Tape peaks from the spectrum of the Er_2O_3 used in this study. The photoluminescence analysis of plain Scotch Brand Tape shows emission peaks at 648 nm, 811 nm, 823 nm, 900 nm, 916 nm, 1621 nm, and 2432 nm. Also seen in this spectrum are peaks from the laser, which appear at 1064 nm, 1596 nm, and 2129 nm. These peaks were found in all of the samples in this study, and they were considered as peaks due to the host. Figure 5.15 shows peaks for the plain Scotch Brand Tape.

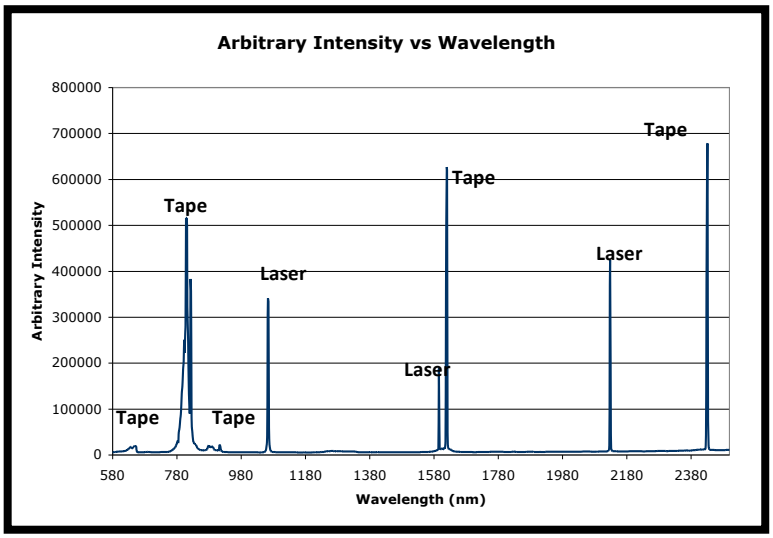

Figure 5.15 Photoluminescence analysis of plain Scotch Brand Tape showing peaks from the tape and the excitation laser.

Er_2O_3 Nanoparticles Adhered to Scotch Brand Tape

The photoluminescence analysis shows that Er_2O_3 Nanoparticles emit at 818 nm when excited by a 532 nm Nd:YAG laser and 783 nm crystal laser. Figure 5.16, shows the 818 nm, peak for Er_2O_3 nanoparticles adhered to Scotch Brand Tape. This peak corresponds to $^4I_{15/2} \rightarrow {}^4I_{13/2}$ transition [32].

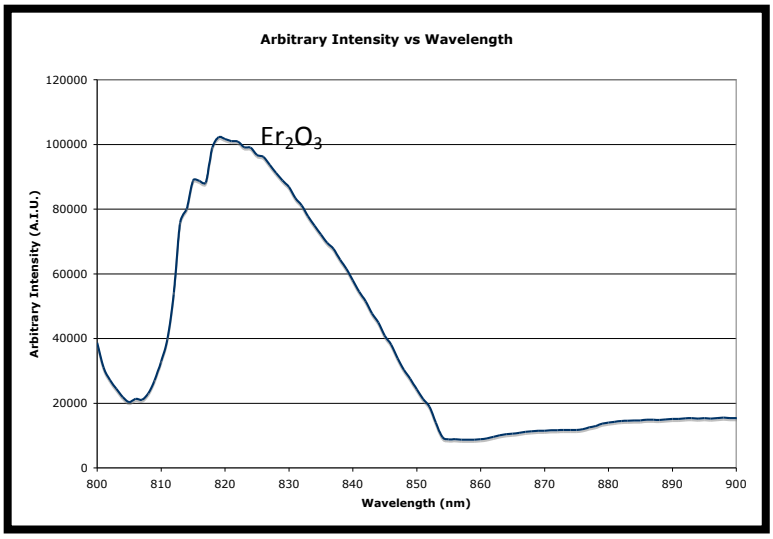

Figure 5.16 The 818 nm peak for Erbium Oxide (Er_2O_3) adhered to Scotch brand tape using the 783 nm excitation laser.

Table 5.5 Statistical analyses data for nanoparticles adhered to Scotch Brand Tape.

Emission Wavelength λ (nm)	**818 nm**
Sample Size (n) [runs]	5
Standard Error (t)	22.33
P-Value (p)	2.38×10^{-5}
Mean (A.I.U.)	112905
Standard Deviation (s) (A.I.U.)	11306
Interval (95%) (A.I.U.)	(98867, 126944)
Null Hypothesis (H_0)	REJECT

The statistical error analysis of the sample showed the peaks at 818 nm were statistically significant. Figure 5.17 shows the 818 nm peak for Erbium Oxide (Er_2O_3) adhered to Scotch Brand Tape. However, due to the peaks from the Scotch Brand Tape at 811 nm and 823 nm, it is uncertain if the peak at 818 nm is actually due to the Er_2O_3

nanoparticles or the Scotch Brand Tape. Because of this, the photoluminescence analysis of the Er_2O_3 nanoparticles on Scotch Brand Tape will be disregarded.

Photoluminescence of Er_2O_3 Nanoparticles in a Vacuum vs Air

The photoluminescence analysis in a vacuum and in air show that Er_2O_3 nanoparticles emit at 554 nm and 813 nm when excited by a 532 nm Nd:YAG laser and 783 nm crystal laser. Figure 5.18 shows the 554 nm and 813 nm, peaks for Er_2O_3 nanoparticles in a vacuum and air. The 554 nm and 813 nm peaks correspond to $^4I_{15/2} \rightarrow {}^4S_{3/2}$ and $^4I_{15/2} \rightarrow {}^4I_{13/2}$ transitions [31, 32].

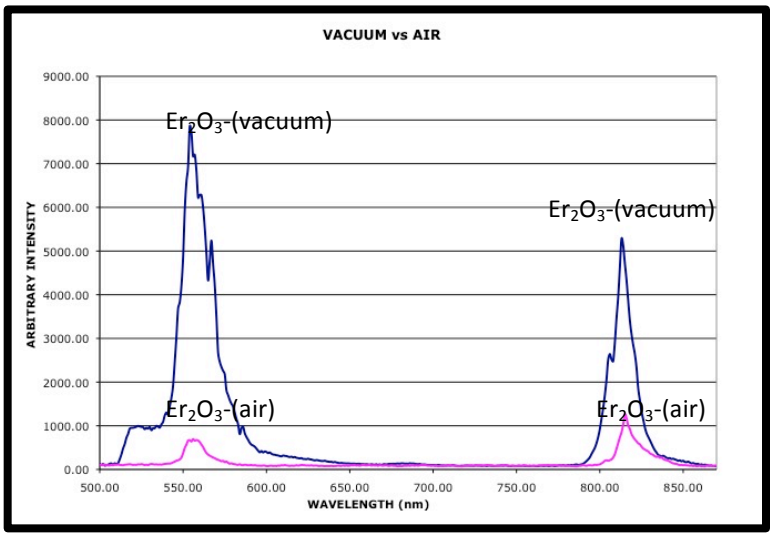

Figure 5.17 Graph of Photoluminescence spectrum showing the Er_2O_3 peaks in Vacuum vs Air. This data was provided by Dr. Martin Kordesch of Ohio University.

Chapter 6

Discussion and Conclusion

Thin Films

The results for each of the thin films are shown in Figure 5.1 through Figure 5.11. The spectral peaks have been assigned based off the conversion from wavelength to energy using the relationship $E\lambda = hc$, where E is energy, λ is the wavelength, h is Plank's Constant (6.626×10^{-34}J·s), and c is the speed of light (2.99×10^{8} m/s).

Holmium (Ho) has several known transitions after being excited by the excitation sources. The excitation of the Holmium (Ho) thin film produced a very weak IR emission at 825 nm, and a strong IR emission at 1537 nm. These peaks were the result of $^5S_2 \rightarrow {}^5I_7$ and $^5S_2 \rightarrow {}^5I_5$ transitions [30]. The peak at 1537 nm was approximately 3.4 times larger than the peak at 825 nm calculated from the mean of each peak.

Samarium (Sm) has several known transitions after being excited by the excitation sources. The excitation of the Samarium (Sm) thin film produced a very weak IR peak at 936 nm, a weak IR peak at 1863 nm. The peak at 1863 nm was approximately 1.2 times larger than the peak at 936 nm, as calculated from the mean of each peak.

Thulium (Tm) has several known transitions after being excited by the excitation sources. The excitation of the Thulium (Tm) thin film produced a strong IR peak at 824 nm, a weak IR peak at 1293 nm, and a weak IR peak at 1891 nm. These peaks were the result of $^3H_4 \rightarrow {}^3H_6$, $^3H_5 \rightarrow {}^3H_6$, and $^3F_4 \rightarrow {}^3H_6$ transitions. The peak at 825 nm was approximately 41.6 times larger than the peak at 1293 nm, and was approximately 33.8 times larger than the peak at 1891nm, as calculated from the mean of each peak.

Each of the AlN rare-earths analyzed all emit in the IR range of the spectrum and can possibly be grown for utilization in night vision technology, thermal imaging, communications, astronomy, tracking technology, meteorology, art history, and heating [28, 29].

Erbium Oxide (Er_2O_3) Nanoparticles

The results for the Er_2O_3 nanoparticles are shown in Figures 5.12 through Figure 5.18. The spectral peaks have been assigned based off the conversion from wavelength to energy using the relationship $E\lambda = hc$, where E is energy, λ is the wavelength, h is Plank's Constant (6.626×10^{-34}J·s), and c is the speed of light (2.99×10^8 m/s).

The Er_2O_3 nanoparticles produce several transitions after being excited by the excitation sources. The excitation of the Er_2O_3 nanoparticles produced a strong yellow peak at 564 nm, a strong orange peak at 603 nm, and a strong IR peak at 814 nm. These peaks were the result of $^4I_{15/2} \rightarrow {}^4S_{3/2}$, $^4I_{15/2} \rightarrow {}^4F_{9/2}$ and $^4I_{15/2} \rightarrow {}^4I_{13/2}$ transitions. The peak at 814 nm was approximately 2.3 times larger than the peak at 564 nm, and was approximately 6.8 times larger than the peak at 603 nm, as calculated from the mean of each peak.

Figure 5.18 shows peaks at 554 nm and 813 nm for the Er_2O_3 nanoparticles in a vacuum and in air. The peak at 554 nm in a vacuum is 11.7 times greater than the same peak in air. The peak at 813 nm in a vacuum is 2.4 times greater than the same peak in air. This analysis shows that the emissions from Er_2O_3 nanoparticles are greater under a vacuum.

Since we have shown that in a vacuum, the nanoparticles will emit more strongly, this makes them a good candidate for cancer detection or internal body cells visualization. If suspected cancerous tissues are analyzed by these nanoparticles under a hypoxic condition, a more clear detection will occur.

References

1. M. Maqbool, I. Ahmad, H. H. Richardson and M. E. Kordesch. Direct ultraviolet excitation of an amorphous AlN:Praesiodimium phosphor by co-doped Gd(+3) Cathodoluminescence, Applied Physics Letters 91, 193511 (2007).

2. M. Maqbool, Martin. E. Kordesch, and A. Kayani, Enhanced Cathodoluminescence from an amorphous AlN:Holmium phosphor by co-doped Gd(+3) for optical devices applications, Journal of the Optical Society of America-B 26, 998 (2009).

3. M. Maqbool, E. Wilson, J. Clark, I. Ahmed and A. Kayani, Luminescence from Cr(+3) doped AlN films deposited on optical fiber silicon substrates for use as waveguides and laser cavities, Applied Optics 49, 653 (2010).

4. N. Managaki, M. Fujii, T. Nakamura, Y. Usui, and S. Hayashi, Enhancement of photoluminescence from Yb and Er co-doped Al_2O_3 films by an asymmetric metal cavity, Appl. Phys. Lett. 88, 042101-042103 (2006).

5. A. J. Steckl and R. Birkhahn, Visible emission from Er-doped GaN grown by solid source molecular beam epitaxy, Appl. Phys. Lett. 73, 1700-1702 (1998).

6. M. Maqbool , H. H. Richardson and M. E. Kordesch, Electron penetration depth in amorphous AlN exploiting the luminescence of AlN:Tm/AlN:Ho bilayers Current Applied Physics 9, 417-421 (2009).

7. V. Dimitrova, P.G. Van Patten, H. Richardson and M.E. Kordesch, Photo-, cathodo-, and electroluminescence studies of sputter deposited AlN : Er thin films, Applied Surface Science 175-176, 480-483 (2001).

8. F. S. Liu, Q. L. Liu, J. K. Liang, J. Luo, H. Zhang, Y. Zhang, B. Sun, and G. Rao, Visible and infrared emissions from c-axis oriented AlN:Er films grown by magnetron sputtering, Journal of Applied Physics 99, 053515 (2006).

9. M.E. Little and M.E. Kordesch, Band-gap engineering in sputter-deposited $Sc_xGa_{1-x}N$ Appl. Phys. Lett. 78, 2891-2893 (2001).

10. John B. Gruber *et al*, Spectroscopic properties of Sm^{3+} ($4f^5$) in GaN. Journal of Applied Physics, Volume 91, No. 5, 2929-2935 (2002).

11. Photoluminescence, Retrieved 29 June 2012 from http://en.wikipedia.org/wiki/Photoluminescence.

12. H. J. Lozykowski, Kinetics of luminescence of isoelectronic rare-earth ions in III-V Semiconductors. Physical Review B 48, 17758 (1993).

13. S. Schmitt-Rink *et al*, Excitation Mechanisms and Optical Properties of Rare-Earth Ions in Semiconductors. Physics Review Letters. 66, 2782 (1991).

14. G. H. Dieke, Spectra and Energy Levels of Rare Earth Ions in Crystals, Interscience Publishers (New York, 1968).

15. B. M. Walsh, N. P. Barnes, and B. D. Bartolo, "Branching ratios, cross sections, and radiative lifetimes of rare earth ions in solids: Application to Tm^{3+} and Ho^{3+} ions in $LiYF_4$", J. Appl. Phys, 83, 2772-2787 (1998).

16. M. Maqbool, Luminescence from thulium and samarium doped amorphous AlN thin films deposited by RF magnetron sputtering and the effect of thermal activation on luminescence, European Physical Journal Applied Physics, 34, 31-34 (2006).

17. Gallium Nitride (GaN), n.wikipedia.org/wiki/Gallium_nitride.

18. Aluminum Nitride (AlN), n.wikipedia.org/wiki/Aluminum_nitride

19. Indium Nitride (InN), n.wikipedia.org/wiki/Indium_nitride

20. Boron Nitride (BN), n.wikipedia.org/wiki/Boron_nitride

21. Karl A. Gschneider, Jr., General Review of Scientific and Technical Aspects of the Utilization of RE Materials, Analysis of Rare Earth Materials, 1-7, (1973).

22. Robert C. Weast, CRC Handbook of Chemistry and Physics, CRC Press, B-243, (1983).

23. Billings, Bruce H. and Gray, Dwight E., American Institute of Physics Handbook Third Edition, Table of Energy Levels of Rare Earth Elements, McGraw-Hill, p7-25, 1972.

24. Appropedia, Nanoparticles for cancer detection and destruction. Retrieved June 4, 2012, from http://www.appropedia.org/Nanoparticles_for_cancer_detection_and_destruction.

25. KK Jain, Advances in the field of nanooncology. BMC Medicine 2010, 8:83.

26. Allan G. Bluman, Elementary Statistics: A Step by Step Approach: Fifth Edition, McGraw-Hill, 2004.

27. Bevington, Philip R, and Robinson, D. Keith, Data Reduction and Error Analysis for the Physical Sciences,(2-15). McGraw-Hill, 2003.

28. eHow, Uses for Infrared Light. Retrieved June 20, 2012, from http://www.ehow.com/facts_5454589_uses-infrared-light.html.

29. Universe Today, Infrared Light by John Carl Villanueva. Retrieved June 20, 2012, from http://www.universetoday.com/34504/infrared-light/.

30. G.A. Newburg er al. Resonanntly diode-pimped Ho^{+3} - Y_2O_3 ceramic 2.1 micrometer laser, Optics Express, Vol. 19, Issue 4, pages 3604 – 3611 (2011).

31. N. Guskos et al. Relative Intensities of f-f Transitions of Erbium(III) Ion Studied by Photoacoustic Spectroscopy, Rev. Adv. Matter. Sci. 23(2010) 97 – 101.

32. Laércio Gnomes et al. Energy level decay and excited state absorption process in erbium-doped tellurite glass. Journal of Applied Physics 110, 083111 (2011).